Atmos. Chem. Phys. Discuss., 10, 7215–7264, 2010
www.atmos-chem-phys-discuss.net/10/7215/2010/

Atmospheric Chemistry and Physics Discussions

This discussion paper is/has been under review for the journal Atmospheric Chemistry and Physics (ACP). Please refer to the corresponding final paper in ACP if available.

Combining visible and infrared radiometry and lidar data to test ice clouds optical properties

A. Bozzo[1,*], **T. Maestri**[1], **and R. Rizzi**[1]

[1]Dipartimento di Fisica, Università di Bologna, Italy
[*]now at: University of Edinburgh, School of GeoSciences, Edinburgh, UK

Received: 5 December 2009 – Accepted: 6 March 2010 – Published: 18 March 2010

Correspondence to: R. Rizzi (rolando.rizzi@unibo.it)

Published by Copernicus Publications on behalf of the European Geosciences Union.

Abstract

Measurements taken during the 2003 Pacific THORPEX Observing System Test (P-TOST) by the MODIS Airborne Simulator (MAS), the Scanning High-resolution Interferometer Sounder (S-HIS) and the Cloud Physics Lidar (CPL) are compared to simulations performed with a line-by-line and multiple scattering modeling methodology (LBLMS). Formerly used for infrared hyper-spectral data analysis, LBLMS has been extended to the visible and near infrared with the inclusion of surface bi-directional reflectance properties. A number of scenes are evaluated: two clear scenes, one with nadir geometry and one cross-track encompassing sun glint, and three cloudy scenes, all with nadir geometry.

CPL data is used to estimate the particulate optical depth at 532 nm for the clear and cloudy scenes. Cloud optical depth is also retrieved from S-HIS infrared window radiances, and it agrees with CPL values, to within natural variability. MAS data are simulated convolving high resolution radiances.

The paper discusses the results of the comparisons for the clear cases and for the three cloudy cases. LBLMS clear simulations agree with MAS data to within 20% in the shortwave (SW) and near infrared (NIR) spectrum and within 2 K in the infrared (IR) range. It is shown that cloudy sky simulations using cloud parameters retrieved from IR radiances systematically underestimate the measured radiance in the SW and NIR by nearly 50%, although the IR retrieved optical thickness agree with same measured by CPL. MODIS radiances measured from Terra are also compared to LBLMS simulations in cloudy conditions using retrieved cloud optical depth and effective radius from MODIS, to understand the origin for the observed discrepancies. It is shown that the simulations agree, to within natural variability, with measurements in selected MODIS SW bands.

The paper dwells on a possible explanation of these contraddictory results, involving the phase function of ice particles in the shortwave.

ACPD

10, 7215–7264, 2010

1 Introduction

A recent review of the light scattering properties of cirrus (Baran, 2009) points out that it is more desirable to construct cirrus ice crystal models that predict the light scattering properties of non-spherical ice crystals that can be applied at any wavelength rather than at particular wavelengths. It also points out that the choice of ice crystal model, beside its importance for climate modeling, is also important for the space-based remote sensing of cirrus properties, since inappropriate choice of the scattering phase function may lead to errors in retrieved optical depth of several factors. The review contains a wealth of references pertaining to this problem.

The issue of the quality of cloud products that are now routinely produced from satellite data is addressed in Ham et al. (2009) that examines the quality of the MODIS retrieved cloud products. These are used as input of a radiative transfer model to compute multiply scattered radiances at a number of MODIS channels and comparing the measurements to the simulations. The main findings are that radiances for shortwave bands between 0.466 and 0.857 µm appear to be quite accurate, while simulated radiances for the 1.24, 1.63 and 3.78 µm bands do not well agree with measurements. Large differences between simulations and data are also found in the infrared window bands (such those centered at 8.56, 11.0 and 12.0 µm).

In Yang et al. (2007) the differences of the bulk optical properties of ice clouds retrieved in MODIS collection 4 and 5 are investigated and it is shown that collection 5 optical thickness over ocean are a factor 1.9 higher than the collection 4 counterpart. Moreover it is stated that the differences can lead to either an enhancement or a reduction of the warming effect of ice clouds, depending on the specific ice cloud of interest.

In the Zhang et al. (2009) paper, the main concern is the influences of different ice particle micro-physical and optical models on the resulting optical thickness retrievals from satellite measurements of solar reflection. They find that the ice cloud optical thickness retrieved from POLDER is substantially smaller than that from MODIS, and the difference is attributed primarily to the difference of asymmetry factor used in the

two retrievals. They conclude that ice cloud optical thickness retrievals based on satellite measurements of solar reflection are highly sensitive to the choice of the ice particle model assumed in the retrieval.

The present study was initiated to evaluate the quality of a forward modeling methodology, called Line-By-Line Multiple Scattering (LBLMS), that is an extension to the shortwave of a state-of-the-art methodology already used to simulate high resolution spectral data in the infrared spectral range, from 3000 to 50 cm^{-1} (Rizzi et al., 2001; Amorati and Rizzi, 2002; Maestri and Rizzi, 2003; Tjemkes et al., 2003; Rizzi and Maestri, 2003; Maestri et al., 2005).

Two diverse data sets are used. The first is a field study during the 2003 Pacific THORPEX Observing System Test (P-TOST, http://angler.larc.nasa.gov/thorpex/), that will be referred to as PTH. During PTH the spectro-radiometric data are combined with lidar products that describe the particulate (aerosol and clouds) extinction profiles. Since our long-term interests are on the retrieval of cloud variables, the experimental cases selected for the core study involve radiances measured in presence of cloud decks. However the methodology and results for two clear scenes are also included, since nadir and cross track simulations of a clear scene provide evidence of correct modeling of the surface and of the aerosol layers, especially in the shortwave (SW) part of the spectrum. This is especially important when dealing with thin clouds in order to avoid that incorrect simulations of surface or aerosols properties affect the cloud properties retrieval process.

The second data set is from the Moderate Resolution Imaging Spectroradiometer (MODIS) and corresponding retrieved cloud products. This data set is used to clarify the unexpected results obtained from the PTH cloud cases, and is not intended to present results of statistical significance.

The description of the experiment and of all the case studies is given in Sect. 2, together with the details of the modeling methodology. The results for the clear PTH case are discussed in Sect. 3, and the three PTH cloudy cases and the MODIS computations are discussed in Sect. 4. A summary with conclusions follows in last section.

ACPD
10, 7215–7264, 2010

2 Description of the experiment and instruments

The PTH data-set was measured on 22 and 23 February 2003 during the flight of the P-TOST over the Pacific Ocean SE of the Hawaiian Islands, when the high altitude NASA aircraft ER-2 carried the three instruments of interest for our analysis: S-HIS, MAS and CPL.

The Scanning High-resolution Interferometer Sounder (S-HIS) (Revercomb et al., 1998) is a Fourier-transform spectrometer with laser-controlled sampling, operating in the thermal spectrum between 3.3 µm and 17.2 µm (3000–680 cm^{-1}); it utilizes a 45°scene mirror that rotates through a measurement sequence consisting of views of the earth and two calibration sources, one at ambient and another up to 60 K above ambient. During each scan, 11 cross-track Field of Views (FOVs) are sampled (±35° total view angle), with a nadir spatial resolution of 2 km from the nominal 20 km ER-2 flight level and a spectral resolution of 0.5 cm^{-1}.

The MODIS Airborne Simulator (MAS) (King et al., 1996) was built as support to the development of the MODIS satellite instrument: it is a 50 channel scanning spectrometer that covers the spectral range from visible to thermal infrared and acquires 50×50 m (at nadir) pixel data across a 37 km swath (±43° view angle) from the nominal ER-2 flight level. At the nominal ER-2 ground speed of 210 m/s, MAS FOVs show an along-track superposition of the scan lines of about 33% of the pixel width.

The Cloud Physics Lidar (CPL) (McGill et al., 2002) provides cloud and aerosol backscatter profile at 30 m vertical and 200 m horizontal resolution at 1064 nm, 532 nm, 355 nm. During the PTH experiment the CPL, provided optical depths at 532 nm up to a saturation value of about 3.

In addition to the ER-2, the NOAA G-4 research aircraft flew carrying the Airborne Vertical Atmospheric Profiling System (AVAPS) to measure the temperature and humidity profiles from cruise level (12 km) to the ground. The ER-2 Mission Report specifies that the aircraft has flown from 21:40 UTC on 22 February to 04:30 UTC on 23 February (11:40 to 18:30 local time) at a cruise altitude of 20 km and the NOAA G-4

ACPD
10, 7215–7264, 2010

took off 20 min after the ER-2. A wide leveled high pressure area was prevailing over the Hawaiian region. The ER-2 flew from Hickam AFB to get on WNW-ESE oriented track line (20° N, 153° W to 16° N, 144° W) designed to enter and transect subtropical jet zone running up from tropics between 150 and 140° W longitude. ER-2 did 2 back and forth runs (4 total segments) of this line with the G-4 doing profiling on a similar but shorter leg, releasing 11 drop-sondes. G-4 flew back after two ER-2 legs. The Western third of this line contained clear to partly cloudy (low cloud) skies. Middle and eastern ends were overcast with thick cirrus associated with the subtropical flow. Transect crossed core of subtropical jet positioned at about 145° W. An overlook of the entire mission's route can be seen in Fig. 1.

2.1 Modeling methodology

Although S-HIS and MAS flew together on the ER-2, the data-recording time of the two instruments had different reference, resulting in different time overpass over the same scene. Moreover, it had been noted (R. Holz, University of Wisconsin, Madison, personal communication, 2004) that S-HIS data had wrong geographic data positioning due to use of the inertial navigation system of the ER-2 as reference, which in the analyzed mission didn't work properly. Therefore a scheme was developed to collocate MAS and S-HIS data using MAS channel 45 (a window centered at 11 µm). This channel performs a relatively more stable measurement of the scene radiance with respect to window channels located in NIR range, which are affected, moreover, by solar contribution. Two sets of virtual measurements are generated, having the spatial resolution of S-HIS and the spectral resolution of MAS: MAS pixels are averaged over the S-HIS footprint closest to nadir and the S-HIS data is convolved over the MAS spectral response function to produce the equivalent MAS spectral bands (Moeller et al., 2003). The minimisation of the mean square differences between the convolved S-HIS signal and the averaged MAS signal is performed over a 750 km long ER-2 track (corresponding to flight between 01:06 UTC and 02:00 UTC on 22 February) in which clear sky, broken clouds and overcast situations are present. The mean temporal displacement

ACPD
10, 7215–7264, 2010

between MAS and S-HIS data is found to be 41±2 s. The uncertainty of 2 s produces a possible spatial displacement of about 400 m at the nominal ground speed of the ER-2, i.e. it is smaller than the linear dimension of the S-HIS nadir footprint.

The simulations are done with a suite of codes collectively called Line-By-Line Multiple Scattering (LBLMS). In the present work the line-by-line computations of layer spectral optical depths are done using the Line-by-Line Radiative Transfer Model (LbLRTM) (Clough and Iacono, 1995). LbLRTM can solve the clear sky radiative transfer equation, but in our study is used to generate layer monochromatic optical depths (OD). These are interpolated at 0.002 cm^{-1} and then convolved to compute spectrally averaged OD. Tests were done to find the appropriate spectral resolution for the specific sensor that is modeled (S-HIS and MAS in this work) so that the difference between radiances convolved using the averaged optical depths or directly the LbLRTM monochromatic radiances were below a given threshold. Results are dependent on the spectral widths over which the OD average is performed and also on the atmospheric layering.

After the tests three different spectral resolutions were used, as a compromise between a reasonable computing time and accuracy: 0.01 cm^{-1} from 580 to 3000 cm^{-1} (3.33–17.2 µm, indicated as IR in this paper), 0.05 cm^{-1} from 3000 to 7000 cm^{-1} (NIR, 1.43–3.33 µm), and 0.5 cm^{-1} from 7000 to 22 000 cm^{-1} (SW, 0.45–1.43 µm). The HITRAN 2004 (Rothman et al., 2005) spectroscopic database and the MT-CKD 1.3 water vapour continuum absorption model (Clough et al., 2005) are used.

The integration of the radiative transfer equation, including multiple scattering, is based on the code RT3 (Evans and Stephens, 1991). Layer spectral absorption optical depth is the sum of molecular and particle absorption and spectral total scattering optical depth is the sum of particle and Rayleigh scattering with the total phase function being a weighted mean of the two components.

The emissivity of the ocean surface in the IR is computed using the method described in Masuda et al. (1988). The ocean surface reflection properties take into account the contribution from the wind-roughened surface (Cox and Munk, 1954), the white caps and the up welling radiation scattered back from below the surface as

ACPD
10, 7215–7264, 2010

function of the oceanic pigment concentration. The model implemented in RT3 is analogous to the one adopted in 6S (Vermote et al., 2006), with the only exception being the wind direction dependency that in RT3, due to limitations inherent to its computational structure, is not allowed. A description of the methods adopted and of the results obtained is found in Bozzo (2009). Post-processing of high resolution radiances to produce un-apodised spectra at S-HIS resolution is done as described in Rizzi et al. (2001). Simulated MAS radiances are obtained by convolving the spectral values at the indicated resolution with the MAS response functions (NASA, cited 2008).

Aerosol single scattering optical depth and phase function are computed using an in-house code, but the main physics contained (refractive index of components, aerosol as a collection of homogeneous spherical particles, size distributions, definition of external mixtures and growth coefficients) is analogous to the package OPAC (Hess et al., 1998) and so are the computed properties. The Mie scattering portion is handled by routines distributed together with the initial version of the RT3 code by Frank Evans.

The retrieval methodology (RT-RET) used to derive cloud optical depths and effective dimension of the cloud particle size distribution (PSD) from S-HIS radiances is described (and applied to Arctic and Mid latitude clouds respectively) in Maestri and Holz (2009) and Maestri et al. (2010). RT-RET uses LbLRTM and the same doubling and adding algorithm (RT3) described earlier.

The single scattering properties for different ice habits in the short-wave (0.25–4.5 µm) and long-wave (4.5–100 µm) spectral ranges are taken from Yang and Liou (1998) and Yang et al. (2005) and will be referred to in the following by the acronyms SSP-SW and SSP-IR.

Previous work (e.g. Wendisch et al., 2005; Wyser, 1999) has shown large differences in simulations based on PSD composed of single shapes and there are no reasons to prefer one shape over another. Our choice is to use a mixture (called MIXML) of different habits, bullet rosettes, aggregates, droxtals and a small percentage of solid columns as described in Bozzo et al. (2008) and Fig. 1 of the quoted paper. MIXML is based on Lawson et al. (2006) measurements, developed in the context of mid latitude

ACPD
10, 7215–7264, 2010

ice clouds. The major differences between mid-latitude and tropical cirrus clouds are found for cirri formed near strong tropical convective events, at the top of large anvils. Such ice clouds present usually higher fractions of larger particles than mid latitude-synoptic ice clouds, associated to strong updrafts (Baum et al., 2005). In case of synoptically generated mid-latitude cirrus, the large ice crystals tend to subside quickly due to the weak updrafts. In our case, although the cirrus is associated with the subtropical jet-stream, it does not show the characteristics related to the tropical convective structures. MIXML has been tested in the analysis of infrared interferometric data collected at Mid Latitudes and in cloudy conditions during the italian phase of the EAQUATE experiment Maestri et al. (2010).

The ice particle size distribution (PSD) adopted for the forward and inverse computations is a Gamma distribution:

$$n(D) = N_0 D^{\mu} e^{-\lambda D} \tag{1}$$

where D is the particle maximum dimension, N_0 is the intercept value of the distribution, λ the slope (with unit of an inverse dimension) and μ is the dispersion (or shape) parameter. The PSD is extended to particles smaller than the maximum dimension for which properties are available in the quoted databases by assuming that in the range from 0 to 2 µm spherical particles are present, whose properties are computed using same code as for aerosol properties.

Particular attention has been given to the treatment of the phase function to account for the sharp diffraction peak exhibited by the ice crystals. Since the scattering phase function is handled with an expansion in Legendre polynomials, such peaked functions would require thousands of components, which in turn would imply an extremely time-consuming solution. Instead the procedure proposed by Potter (1970) has been followed and the phase function peak is modified, with a spectrally varying algorithm which is tailored to minimise the number of Legendre terms required for an accurate reconstruction. In addition we account for the contribution of the delta-transmission peak associated with the forward scattering at a 0°(Takano and Liou, 1988).

The number of Legendre terms used in the computation is linked to the number of angles employed in the zenith discretization in each hemisphere (N_u). After considerable tests we have used, for the ice cloud cases, $N_u = 32$ (and 125 Legendre terms) in all spectral regions except from 600 to 4850 cm^{-1} where N_u is set to 60 (237 Legendre terms). Since the CPU time required for LBLMS computation is proportional to the cube of N_u, the accurate computation of high resolution radiances has required a massive computational effort that was made possible only after code parallelisation.

3 Description of the clear cases and results

3.1 Measurement conditions for the clear cases

Figure 2 illustrates the scene under consideration: the left panel is MAS channel 45 (11 µm) and the right panel is an RGB image from three MAS channels. A widespread sun-glint-affected region is observed and clearly distinguishable in the right panel along the full scan. Two regions are selected for the nadir and cross-track comparisons. For the nadir case the measured MAS data are averaged over a 20 pixel wide and 400 pixel long area, which covers a section 2° wide (±1° across the nadir line) and roughly 15 km long, along the blue line in Fig. 2. For the cross-track case MAS measurements are averaged over an area as wide as the full MAS swath and 120 pixel long (the red box on Fig. 2), which roughly corresponds to a 4 km long and 40 km wide region.

In both case studies the averaged MAS data is compared to the LBLMS simulation. The solar zenith angle is approximately 31°and solar azimuth 204°; sensor azimuth angle swings between 204 and 24°, hence aligned with the surface incidence plane of solar radiation.

Three drop-sondes were launched in coincidence with this track: one at 23:07 UTC, the second at 23:12 UTC and the third at 23:17 UTC. All drop-sondes measured a 10 m wind speed between 6 m/s and 7 m/s with azimuthal direction around 30°, hence slightly skewed with respect to the instrument-sun plane: wind speed has been set

ACPD
10, 7215–7264, 2010

in the simulation at 6.5 m/s. The vertical profile of temperature and humidity used for the simulation is a composite of the data from the 23:17 UTC drop-sonde and a standard tropical profile (Anderson et al., 1986) to fill the 10 km gap between the G-4 and the ER-2 cruise altitude. The CO_2 mixing ratio profile is modified to measured global mean value for the period of the campaign. Absorption from chloro-fluoro-carbon macro molecules (CFC) is also accounted for.

The CPL detected the presence of an aerosol layer distributed in the boundary layer from 1000 m down to about 500 m. Below this level there is no information on aerosol optical depth. Since the source of aerosol is the oceanic surface an exponential extrapolation of the measured optical depth profile down to the marine surface is assumed. The integrated optical depth at 532 nm obtained with this procedure is 0.07. The aerosol layers (from surface to 1000 m height) are simulated with the optical characteristics of a maritime tropical aerosol model (same mixture defined in Hess et al. (1998), grown in an ambient with 80% relative humidity, in accordance with the drop-sondes measurements.

The pigment concentration of the oceanic water derived from the global products of the SeaWiFS satellite (Johnson et al., 1998), averaged over 8-days around the 22 February 2003 in the Pacific Ocean SE of the Hawaiian Islands, has a mean value of 0.07 mg/m^3.

3.2 Results for the clear nadir case

Results for the nadir case are shown in the three panels of Fig. 3 in terms of radiance (all radiance values are given with unit W/(m^2 µm sr)) for the SW and NIR and brightness temperature (K) for the IR range. Figure 4 shows the relative errors in radiance between LBLMS and MAS data for the SW and NIR range and the absolute error in brightness temperature (K) for the IR range. The error bars added to the measured values represent one standard deviation of MAS data and denote the overall scene variability (comprehensive of radiometric errors). In this case the error bars are barely noticeable due to the stable signal provided by the clear sky scene. The channel

ACPD
10, 7215–7264, 2010

centered at 1848 cm^{-1} did not work properly during the selected mission and should be ignored in the comparison.

The difference between the simulations and the MAS data is almost constant in the SW range between 0.45 and 1 µm with a value of about 1.5 $W/(m^2\,\mu m\,sr)$, hence the relative error increases with increasing wavelength since the radiance level is decreasing: it remains below 10% for wavelength shorter than 0.7 µm and it grows up to 35% approaching the channels at 0.95 µm. In the NIR range the relative error is around 10–15% with the exception of the strong H_2O band, where it reaches values of about 90%.

In the IR, from 500 cm^{-1} to 2800 cm^{-1}, the absolute errors are between 0.5 and 2 K except in the 3 channels located in the strong CO_2 absorption bands (one at 700 cm^{-1} and the other two at 2250 and 2450 cm^{-1}). The discrepancy in the opaque channels due to CO_2 absorption is certainly linked to the assumed atmospheric temperature profile . The surface skin temperature is set equal to the last temperature measured by the drop-sonde and this affects the simulation in the window regions. These differences could be easily eliminated to a large extent by improving the assumed atmospheric/surface temperature profile: these fitting procedures are however more pertinent when a product is to be obtained rather than when a detailed case study is examined.

The largest relative differences in the SW and NIR are found in channels with important water vapour absorption. We have performed simulations also of the S-HIS data (not shown) and the results show a negative bias (the simulation being colder that the S-HIS data) in the infrared vibro-rotational band of water vapour. Therefore the water vapour profile, and in particular the profile assumed between the G-4 and the ER-2 flight levels, is likely more humid than the true profile, which also explains the negative bias in the SW and NIR channels.

In conclusion the main causes of the observed discrepancies in the SW and NIR could be the modeling of the scattering by the oceanic surface, the assumed aerosol optical depth vertical profile, the aerosol mixture adopted and its growth properties. Each of these will be discusses in what follows.

To understand the importance of each process, the four panels of Fig. 5 show the upwelling radiance at MAS height simulated for four channels when a) the source function is the surface with a molecular atmosphere that only absorbs radiance (line labeled SUR in all panels), b) when molecular scattering is added as source of radiance (SUR+RAY) and finally c) when aerosol is also present (FULL). It is evident that in our case study the surface and molecular scattering are the dominant radiation sources.

Currently our modeling of the oceanic surface assumes that the sun glint pattern is independent on the wind direction. Comparisons with the 6S model indicate that this hypothesis gives an error in the range 10–20% of the signal for low solar zenith angles (Bozzo, 2009). In particular, in case of a zenith angle of 31° the up-welling radiation is enhanced if the wind is blowing along the incident and reflected solar beam plane, whereas it is reduced in case of a wind blowing orthogonal to the sun's reflection plane. The wind's azimuthal angle retrieved from the drop-sondes measurements is around 60°, hence 36° from the sun's reflection plane, which lies along the 24–204° azimuthal line.

The OPAC standard Maritime tropical aerosol model is an external mixture of three components, one of which, the sea salt coarse mode (SSCM) accounts for 1.4% of the mass of the mixture. The extinction optical depth has a maximum around 5 µm decreasing toward shorter wavelengths, markedly different from the sea salt accumulation mode component (SSAM) which has a maximum around 1 micron. Therefore one could devise a slightly different mixture, by increasing the mass of the SSCM and reducing the mass of SSAM, and the new mixture would reduce the underestimation observed in the NIR. Also data on condensational growth by aerosol components is sparse, and it is well known that assuming aerosols are spherically homogeneous particles is only a rough approximation. However the relevance of the aerosol contribution

ACPD
10, 7215–7264, 2010

is so small in this case study that it is not necessary to dwell on the various sensitivity tests performed.

In conclusion the overall agreement of LBLMS simulations to MAS data appears to be good (mostly within 20% in the SW and NIR and 2 K in the IR), and certainly consistent with the approximations used. The small underestimation of LBLMS simulations with respect to MAS measurements in the SW can be related to the simplification of a wind direction independent bidirectional reflectance (BDRF).

In the next section we examine the same scenario, but from different viewing angles.

3.3 Results for the clear cross-track case

LBLMS is tested with a full MAS cross-track scan swinging in the analyzed scene from the maximum to the minimum of the glint reflection region, along the reflection plane of the incoming solar radiation. Up-welling radiation at 20 km is simulated at 32 zenith angles for each hemisphere using 64 terms of the azimuthal-mode Fourier expansion. Pigment concentration, aerosol profile, model and relative humidity are same for the nadir case. Figure 6 shows the reflectance at 20 km for 4 MAS channels defined in the previous section. The BDRF for various wavelengths is computed from averaged MAS data (full lines) inside the red box in Fig. 2, and from LBLMS simulations (dashed lines).

The peak in reflectance is reached for all the 4 curves at around 36°, slightly shifted toward the horizon from the Fresnel reflection point that is supposed to be at the incidence angle of 31°. The glint pattern appears to be less steep and slightly more skewed towards the horizon in the MAS observations: in fact some difference in the glint pattern is expected due to the assumption of a wind direction-independent BDRF in the simulations.

The relative difference are between −10 to +10% over the whole scan for the SW channels, with a larger underestimation for the NIR channels, and are largest in the direction opposite to the reflection point, at minimum MAS radiance values.

ACPD
10, 7215–7264, 2010

4 Description of the cloudy cases and results

4.1 Measurement conditions for the three cloudy cases

As already mentioned the ER-2 did 4 segments and the middle and eastern end of the flight leg were characterized by an extended cirrus associated with the subtropical jet-stream. The transect crossed the jet at about 145° W and 19–20° N. The ER-2 made two back and forth overpasses over the high, thick tropical cirrus.

As pointed out in the discussion of the clear cases, some assumptions adopted in the ocean's reflectivity model implemented in LBLMS could lead to spurious effects in the interpretation of the upwelling radiance, especially at low sun zenith angles. For this reason all measurements between the ER-2 take off time and 24:00 UTC (14:00 local time) were disregarded. The chosen transect is located between 01:26–01:34 UTC and is characterized by a solar zenith angle of 57°.

Thermal infrared and visible MAS imagery show (see Fig. 7) that the cloud is fairly homogeneous only in the optically thickest part and quite variable elsewhere. The thinnest part, located at the edge of the very extended cloud layer, is rather inhomogeneous with many open gaps over the underlying ocean. Some small cumulus clouds can be spotted below the cirrus layer, although not directly beneath the flight line.

Being the flight of the NOAA G-4 much shorter than the ER-2's mission, the dropsonde spatially closest to the data analyzed was launched at 23:27 UTC, hence 2 h before the chosen ER-2 sector, but from satellite imagery there seem to be no important cloud development in these two hours. In the humidity profile, the cloud layer position is characterized by a net increase of relative humidity between 200 hPa and 300 hPa up to a value of 60% in the middle of the layer for the section with the optically thickest cloud. As in the clear sky case, a sub-tropical climatological standard profile is used to fill the gap between the two aircrafts. As an estimate of the surface wind speed we use the same wind speed adopted in the clear sky scene (6.5 m/s), though the relative importance of the surface wind in absence of a sun glint is very small. The

ACPD
10, 7215–7264, 2010

pigment concentration and the aerosol optical depth, profile and mixture are the same adopted in the clear sky case.

For layers with optical depth at 532 nm less than 3, CPL data is used to characterize the internal cloud structure and to define top and bottom cloud levels. Figure 8 shows the extinction cross section at 532 nm at nadir for the flight stretch chosen for the comparison. The cloud becomes thicker and the top height increases while flying from the edge of the cloud layer to the inner part.

The CPL optical depth at 532 nm is shown in Fig. 9 and it is seen that from 01:32 UTC the CPL signal is saturated, hence the cloud bottom information is not reliable. Three sectors are selected from the whole track: they are representative of a very thin (between red lines in Fig. 9), a medium thin (green lines) and a moderately thick (blue lines) cirrus layer.

Cloud optical thickness (OT) and effective dimension D_e are retrieved using RT-RET , applied to averaged S-HIS data, collocated with MAS data, over each of the three sectors highlighted in Fig. 9.

The retrieval methodology RT-RET can be based on any ice crystal shape, but since no measured data is available from the field campaign about the micro-physical composition of the cirrus layer, we have used MIXML, for reasons already discussed.

The size distribution is described by a Gamma with a value of $\mu = 0$. Cloud top and cloud bottom are the average in each sector of the values determined from CPL measurements collocated with S-HIS FOVs. The ice mass (IWC) is assumed to be distributed uniformly over the whole depth of the cloud to match the integrated OT retrieved by RT-RET. In regions where the CPL signal is not saturated, the extinction profile could be used to infer the IWC vertical distribution (assuming a vertically invariant constant composition and size distribution). Comparisons (not shown) between the upwelling radiance computed with an uniform distribution of ice mass and a distribution derived from the lidar-observed extinction profile show indeed some sensitivity, especially in the IR range. However, in order to be consistent with the retrieval procedure and within the three cloud regions (a CPL-based IWC profile is applicable only to the

ACPD
10, 7215–7264, 2010

first 2 sectors), we decided to maintain a uniform IWC profile for all the simulations performed.

Table 5 summarizes the characteristics of each cloud scene. The effective diameter retrieved by RT-RET is in the range 64 to 80 µm, therefore the bulk of the mixture is a combination of the optical properties of irregular aggregate of hexagonal columns and 3-dimensional bullet rosette. The retrieved OT in the IR range is used to determine the total ice mass for the whole depth of the cloud (IWP) and then used to compute the OT at 532 nm using the same PSD, type of mixture and optical properties database: such OT values agree within the natural variability of the OT values derived from CPL, also shown in Table 5, in the three sectors.

4.2 Results for the cloudy cases

LBLMS is used to simulate the upwelling radiance from the three sectors highlighted in Fig. 9 over the whole spectral range covered by MAS, using the same configuration as in the clear sky case.

As for the clear sky case, the MAS channel located at 1848 cm^{-1} did not work properly. In this case we substituted the biased MAS channel with the S-HIS data convolved with the MAS instrumental response function, since the agreement between the instruments is excellent, as shown in Fig. 10 throughout most of the IR spectrum.

Figures 11, 12 and 13 show the comparison between MAS measurements and LBLMS simulations in the three cloud sectors. Figure 14 shows the relative difference between LBLMS simulations and MAS measurements.

Since the procedure RT-RET is based on an iterative least square fit of the S-HIS radiance between 820 and 980 cm^{-1} the agreement between the observations and the simulations in that range is obviously quite good. Agreement between data and simulations (accounting for one standard deviation of the MAS data) is in fact found between 1200 and 650 cm^{-1}, in all the sectors. The difference between LBLMS and MAS lies between −2 K and +2 K, with an overestimation for the thin cloud and a slight underestimation for the other two cases, but well inside the signal variability over the

ACPD
10, 7215–7264, 2010

scene, represented by one standard deviation of the MAS data around the mean value. All the simulations show a narrow overestimation region at about 1050 cm^{-1} due to incomplete information about the O_3 atmospheric profile. For wavenumber greater than 1800 cm^{-1} the signal is the sum of the radiation emitted at terrestrial temperatures and of the reflected solar radiation and the influence of the latter is evident in the spectral ranges where the brightness temperature is higher than that observed in the IR window. LBLMS underestimates MAS in the red and green sectors between 2000 and 2200 cm^{-1}, while overestimates in the blue sector between 2300 and 2700 cm^{-1}

The SW upwelling radiance computed by LBLMS for the three cloudy sectors (Fig. 11, and top panel of Fig. 14) show a strong underestimation with respect to MAS. The difference between LBLMS and MAS for the thick cloud is between 20 to 45% and the difference for the thin cloud is between 25 to 55% relative to MAS. A large underestimation is also seen in the NIR range (Fig. 12 and middle panel of Fig. 14), in all sectors at all wavelengths, ranging from 50 to 60%.

Small particles are strong scatterers of solar radiation, though they bring small contribution to the total PSD's mass and one could imagine that one of the causes of the radiance underestimation is due to an improper treatment of the PSD in the small particle range.

There is in fact much discussion on the role of small ice particles (whose effective diameter is smaller than about 50 to 60 µm) and on the physical mechanisms that produce and eventually maintain these particles inside cirrus clouds. Jensen et al. (2009) report on new aircraft measurements in anvil cirrus sampled during the Tropical Composition, Cloud, and Climate Coupling (TC4) campaign with the 2-Dimensional Stereo (2D-S) probe, which can detect particles as small as 10 µm. They suggest that microphysical measurements in tropical cirrus clouds obtained with the CAS (Cloud Aerosol Spectrometer) should be considered suspect when large crystals are present, and that measurement made with instruments at the wing-hatch location are presumably also affected by shattering artifacts. They however point out that their findings are relevant for relatively low and warm tropical cirrus and do not imply that small crystals do not

play a significant role in the radiative properties of other types of cirrus, such as anvils generated by continental convection, mid-latitude cirrus, or even anvil cirrus in other tropical regions. They also point out that small particles could persist in uppermost tropical tropopause which is often saturated with respect to ice.

We performed various simulations assuming PSD with over- and under- exponential gamma types, both for the retrieval of the cloud optical depth and effective diameter and in the forward simulations. These tests, considering all spectral ranges from SW to IR, do not show any notable improvement on the results already presented since the observed underestimation in our simulation would be reduced only with the inclusion of a number of small particles that would definitely worsen the results in the IR range. We also did tests using different PSDs, each composed of single ice habits (i.e. hollow columns, bullet rosettes, aggregates and plates), but the conclusion we reached were very similar to the one documented in the present study. Some of these sensitive studies can be found at Rizzi et al. (2007).

4.3 A MODIS case study: a cross check for the LBLMS results in the SW and NIR

The MODerate resolution Imaging Spectroradiometer (MODIS) is on-board the NASA polar orbiting Satellites TERRA (EOS AM) and AQUA (EOS PM) (NASA-GSFC, cited 2008).

The scene over the Indian Ocean, observed by MODIS on Terra the 19 January 2009 (granule MOD021KM.A2009019.0320.005.2009019145552), is characterised by a large cirrus located SW of Australia, extending between latitude 40 and 45°(see Fig. 15).

The MODIS cloud mask ensures the ice phase of the cloud. Only pixels with OT much larger than 1 are considered, in order to minimise the influence of the surface properties and of the atmospheric profile below the cloud layer, given the difficulty to obtain an accurate description of their properties. Using MODIS cloud products three small areas are chosen, within the red circle, with different cloud OT; within each area several pixels with same retrieved OT and effective radius R_e are averaged.

ACPD
10, 7215–7264, 2010

The relevant parameters of the three areas and the retrieved properties from MODIS, used for the LBLMS computations, are summarised in Table 5, where the effective diameter is defined as $D_e = 2R_e$ and decreases as the cloud OT increases.

The columns labelled "Sun z.a", "Azi" and "Zen" provide the mean values of the solar zenith angles, and of the azimuth and zenith observation angles used for the LBLMS computations. All the D_e values are quite similar to the D_e used in the PTH simulation, hence the balance of the various components of the mixture MIXML and the PSD are compatible with the one used in the previous section. The column labelled OT 1σ is the error estimate of the OT as given in the MODIS file, and it is understood to be comprehensive of all sources of errors in the retrieval of all parameters that are required to the determination of the OT: cloud top level, cloud phase and effective radius.

The database of ice crystals optical properties are SSP-SW and SSP-IR, same used for the simulations of the PTH case. The standard mid latitude summer profile (Anderson et al., 1986) is used as input to LBLMS, with a surface wind of 5 m/s and an ocean pigment concentration of 0.07 mg/m^3. Since cloud base height is not a MODIS standard product, a cloud geometrical thickness of 3790 m has been assumed with a homogeneous IWC vertical distribution.

The test is done in 9 MODIS bands located in the SW and NIR, defined in Table 5. The results in the IR range would have been difficult to interpret due to the strong dependence of radiance on the accurate reconstruction of the temperature profile and of cloud top height and thickness.

LBLMS computation are done using same technical choices already discussed, in the spectral ranges that cover the MODIS Terra Relative Spectral Response (RSR) for the selected MODIS bands. These RSR are computed as the average (over all channels) of the individual L1B in-band RSRs, that are available from the MODIS Characterization Support Team (MCST) at the address: http://mcst.gsfc.nasa.gov/l1b/. Figures 16, 17 and 18 summarise the results of the comparisons for the three areas described in Table 5.

ACPD
10, 7215–7264, 2010

In these figures the upper panels are radiance differences and the lower panels are the fractional radiance differences (expressed as percentage) that coincide with fractional reflectance differences. The blue bars denote the (2σ) variability around the mean measured radiance, that corresponds to same retrieved OT (and R_e), but slightly different Sun zenith angles and observation angles among the pixels whose radiance is averaged.

Band-2 located at 856.7 nm is currently used for the retrieval of the cloud OT above the ocean (King et al., 1997) and the simulations are very close to measurements at this wavelength. This result would be quite obvious were the same procedure used for the forward and inverse computations. In the present case the result is not obvious and in fact it demonstrates that the inverse (MODIS processing) and forward (LBLMS computations) procedures (single-scattering databases and PSDs) are compatible.

As we move to shorter wavelength some degradation is observed which is always within the stated 2σ uncertainty level, except for Band-3 in Area Ci1, the case of least opacity, where LBLMS overestimates the measured radiance by 20%. In all the cases under study LBLMS overestimates the radiance measured in Bands-6 and 7, which are used to retrieve the effective radius. Although the relatively large relative discrepancies (lower panels) are associated to low radiance values, still they indicate that some of the assumptions on which the LBLMS simulations are based are different from the one used in MODIS retrievals; or that, perhaps, R_e retrieved from band 7 is representative of the top-to-middle part of the cloud and some of the difference could be related to inhomogeneous vertical distribution of particle sizes. We have no firm explanation of this discrepancy and further work is necessary.

5 Summary and conclusions

Measurements taken during the 2003 Pacific THORPEX Observing System Test by the MODIS Airborne Simulator (MAS), the Scanning High-resolution Interferometer Sounder (S-HIS) and the Cloud Physics Lidar (CPL) are compared to simulations with

a line-by-line and multiple scattering modeling methodology (LBLMS). The extension of LBLMS to the visible and near infrared and the treatment of the bi-directional reflectance properties of the marine surface are discussed. A number of scenes are evaluated: two clear scenes, one with nadir geometry and one cross-track encompassing sun glint, and three cloudy scenes, all with nadir geometry. CPL data is used to estimate the particulate optical depth at 532 nm for the clear and cloudy scenes. Cloud optical depth is also retrieved from S-HIS infrared window radiances, and compares well to CPL values. MAS data is simulated convolving high resolution radiances.

The paper discusses the results of the comparisons for the clear cases and for the three cloudy cases. The main (problematic) result is that the simulations in cloudy sky conditions, using cloud parameters retrieved from infrared radiances, systematically underestimate the measured radiance in the visible and near infrared by nearly 50%, while cloud optical depths retrieved from infrared data agree, to within natural variability, with those derived from the lidar.

In order to understand the cause for the observed discrepancies, MODIS radiances measured from Terra are also compared to LBLMS simulations in cloudy conditions using retrieved cloud optical depth and effective radius from MODIS. Three case studies are selected corresponding to cloud decks of various opacity and the attention is focused on SW MODIS bands. The relative differences are lower than ±10% except for B3 for the least opaque cloud where the difference is +18%.

The paper provides evidence that 1) LBLMS simulations in clear conditions are close to (PTH) MAS measurements over the oceanic surface, under a number of diverse viewing geometries; 2) LBLMS simulations in cloudy conditions strongly underestimate MAS radiances in the SW and NIR when cloud parameters are derived from infrared retrievals or lidar measurements; 3) LBLMS simulations are in good agreement with MODIS short-wave measurements when cloud parameters derived from same MODIS data are used to define the cloud optical properties; finally 4) the OTs retrieved by RTRET from S-HIS IR data in 2) agree to within natural variability with OT measured by CPL at 532 nm (see Sect. 5).

ACPD
10, 7215–7264, 2010

The main difference between the results 2) and 3), presented in Sects. 4.2 and 4.3, is that in the former the cloud properties used for the radiance simulation are retrieved from hyper spectral S-HIS measurements in the main IR window, while in the latter they are retrieved from MODIS short wave channels. The two retrieval types sense different properties to derive their product: the MODIS retrieval uses scattered radiation and a realistic description of the phase function is thus fundamental. On the other hand RT-RET uses emitted and scattered radiation to infer the extinction OT. In this last case, scattering is a small fraction of the total signal observed, although it must, and is, fully accounted for by RT-RET. It is therefore expected that best results in the PTH cloudy case study are to be obtained in the IR, while we have found that the best results in the MODIS case study are at wavelengths closest to the one used for the retrieval, i.e. at 856.7 nm.

The retrieval of optical thickness from lidar systems exploits shortwave (scattered) radiation, but generally no assumptions on the phase function is required in the retrieval procedure. Several studies in fact have shown that infrared retrieved optical depths well agree with lidar OT (e.g. Maestri and Holz, 2009; Turner and Eloranta, 2008; DeSlover et al., 2003). In our study the good agreement between CPL OT and RT-RET OT implies that the angularly integrated properties (coefficients of scattering and extinction) are indeed coherent going from infrared to the short wave.

Hence the strong radiance (hence reflectance) underestimation in the SW and NIR obtained in the PTH case studies seems likely caused by the structure of the phase function in the short-wave and the infrared domain. We have taken the utmost care to reconstruct the phase function as originally computed and distributed, therefore the problem lies in some lack of coherence between the original phase function as provided in SSP-SW and SSP-IR.

In Ham et al. (2009), quoted also in the introduction, the RT model DISORT is used to check the consistency of the MODIS cloud products over a broad spectral range, from the IR to the SW. When the MODIS cloud products are used as input parameters in DISORT, there is agreement for the SW channels, a strong overestimation of

ACPD
10, 7215–7264, 2010

the simulated reflectance in the 1.38 µm channel and a strong underestimation of the brightness temperature in all IR channels. The discrepancy found in the IR channels, when the cloud optical properties are retrieved in the SW range, resembles the results from our PTH case study. In Ham et al. (2009) it is pointed out that a possible explanation (page 1603) could be an incorrect retrieval of the actual cloud top, leading to errors in the positioning in the profile and hence in the emission temperature, but the cloud optical properties could also play a not negligible role. In our PTH case study a measurement of cloud top height is available, while it was decided not to model MODIS IR channels, for reasons explained in the main text.

The causes of our problematic results could be multiple and the authors do not have the practical knowledge required to master the fine details of the computations that were required to generate the SSP-SW and SSP-IR databases. The use, in the two spectral ranges, of different methodologies to compute the volume and projected area, that define the geometry of an ice particle of same maximum dimension, could be one of the reasons for the observed discrepancies. A lot of effort is spent in improving the optical properties of ice crystals: the effect of the inclusion of air bubbles inside ice particles is being studied (Xie et al., 2009) as well as changes to surface texture (Yang et al., 2008b) and roughness (Yang et al., 2008a).

In Zhang et al. (2009) it is shown that ice clouds OT inferred from POLDER are substantially smaller than the one inferred from collocated MODIS data, and it is stated that this difference is due to the use of different ice particle scattering models and specifically to the different scattering phase functions. Our results are along the same line, but using a different dataset and simulation methodology. In the conclusion section of Zhang et al. (2009) it is suggested that a set of existing or newly developed ice particle models should be used as the common basis to derive climatologies from satellite measurements. Although this unification is an important step, it represents a necessary but not a sufficient condition. Indeed cirrus clouds pose a fundamental problem because it is the difference in properties among the shortwave and the longwave that is ultimately important, and not only for climate change research. Therefore

ACPD
10, 7215–7264, 2010

the first and most important step is to generate a database of ice particle properties that describes consistently the cloud features that are observed from the SW to the IR.

Acknowledgements. Thanks to Enrico Rossi for his decisive contribution to the parallelisation of the LBLMS code.

References

Amorati, R. and Rizzi, R.: Radiances simulated in the presence of clouds by use of a fast radiative transfer model and a multiple-scattering scheme, Appl. Optics, 41, 1604–1614, 2002. 7218

Anderson, G. P., Clough, S. A., Kneizys, F. X., Chetwynd, J. H., and Shettle, E. P.: AFGL Atmospheric constituent profiles (0–120 km), Tech. rep., Air Force Geophysics Laboratory, Optical Physics Division, Hanscom AFB, aFGL-TR 86-0110, 1986. 7225, 7234

Baran, A. J.: A review of the light scattering properties of cirrus, J. Quant. Spectrosc. Ra., 110, 1239–1260, 2009. 7217

Baum, B. A., Heymsfield, A. J., Yang, P., and Bedka, S.: Bulk scattering properties for the remote sensing of ice clouds. Part I: Microphysical data and models, J. Appl. Meteorol., 44, 1885–1895, 2005. 7223

Bozzo, A.: Atmospheric radiative transfer in multiple scattering conditions. Application to NWP models, Ph.D. thesis, University of Bologna, Bologna, 2009. 7222, 7227

Bozzo, A., Maestri, T., Rizzi, R., and Tosi, E.: Parameterization of single scattering properties of mid-latitude cirrus clouds for fast radiative transfer models using particle mixtures, Geophys. Res. Lett. 35, l16809, doi:10.1029/2008GL034695, 2008. 7222

Clough, S. A. and Iacono, M. J.: Line-by-line calculations of atmospheric fluxes and cooling rates II: Application to carbon dioxide, ozone, methane, nitrous oxide, and the halocarbons, J. Geophys. Res., 100, 519–535, 1995. 7221

Clough, S. A., Shephard, M. W., Mlawer, E. J., Delamere, J. S., Iacono, M. J., Cady-Pereira, K., Boukabara, S., and Brown, P. D.: Atmospheric radiative transfer modeling: a summary of the AER codes, J. Quant. Spectrosc. Ra., 91, 233–244, 2005. 7221

Cox, C. S. and Munk, W. H.: The measurement of the roughness of the sea surface from photographs of the sun's glitter, J. Opt. Soc. Am., 44, 838–850, 1954. 7221

DeSlover, D. H., Turner, D. D., Whiteman, D. N., and Smith, W. L.: Ground-based measurement of cirrus cloud optical properties as validation to aircraft- and satellite-based cloud studies, Proc. SPIE, http://link.aip.org/link/?PSI/4882/205/1, 4882, 205–211, doi:10.1117/12.462372, 2003. 7237

Evans, K. F. and Stephens, G. L.: A new polarized atmospheric transfer model, J. Quant. Spectrosc. Ra., 46, 412–423, 1991. 7221

Ham, S. H., Sohn, B. J., Yang, P., and Baum, B. A.: Assessment of the quality of MODIS cloud products from radiance simulations, J. Appl. Meteorol. Clim., 110, 1591–1612, doi: 10.1175/2009JAMC2121.1, 2009. 7217, 7237, 7238

Hess, M., Koepke, P., and Schult, I.: Optical properties of aerosols and clouds: The software package OPAC, Bull. Am. Meteorol. Soc., 79, 831–844, 1998. 7222, 7225

Jensen, E. J., Lawson, P., Baker, B., Pilson, B., Mo, Q., Heymsfield, A. J., Bansemer, A., Bui, T. P., McGill, M., Hlavka, D., Heymsfield, G., Platnick, S., Arnold, G. T., and Tanelli, S.: On the importance of small ice crystals in tropical anvil cirrus, Atmos. Chem. Phys., 9, 5519–5537, 2009, http://www.atmos-chem-phys.net/9/5519/2009/. 7232

Johnson, B. C., Fowler, J. B., and Cromer, C. L.: The SeaWiFS Transfer Radiometer (SXR), Tech. rep., edited by: Hooker, S. B. and Firestone, E. R., NASA Goddard Space Flight Center, Greenbelt, Maryland, NASA Tech. Memo. 1998–206892, Vol. 1, 1998. 7225

King, M. D., Menzel, W. P., Grant, P. S., Myers, J. S., Arnold, G. T., Platnick, S. E., Gumley, L. E., Tsay, S.-C., Moeller, C. C., Fitzgerlad, M., Brown, K. S., and Osterwisch, F. G.: Airborne scanning spectrometer for remote sensing of cloud, aerosol, water vapor, and surface properties, J. Atmos. Oceanic Technol., 13, 777–794, 1996. 7219

King, M. D., Tsay, S. C., Platnick, S. E., Wang, M., and Liou, K. N.: MODIS Algorithm Theoretical Basis Document, No. ATBD-MOD-05 MOD06 Cloud product, Tech. rep., NASA MODIS Science Team, 1997. 7235

Lawson, R. P., Baker, B. A., Pilson, B., and Mo, Q.: In situ observations of the microphysical properties of wave, cirrus, and anvil clouds. Part II: Cirrus clouds, J. Atmos. Sci., 63, 3186–3203, 2006. 7222

Maestri, T. and Holz, R. E.: Retrieval of cloud optical properties from multiple infrared hyperspectral measurements: a methodology based on a line-by-line multiple scattering code, IEEE T. Geosci. Remote, 47, 2413–2426, 2009. 7222, 7237

Maestri, T. and Rizzi, R.: A study of infrared diabatic forcing of ice clouds in the tropical atmosphere, J. Geophys. Res, 108, 4139–4154, 2003. 7218

Maestri, T., Rizzi, R., and Smith, J. A.: Spectral infrared analysis of a cirrus cloud based on Airborne Research Interferometer Evaluation System(ARIES) measurements, J. Geophys. Res.-Atmos., 110, D06111, doi:10.1029/2004JD005098, 2005. 7218

Maestri, T., Di Girolamo, P., Summa, D., and Rizzi, R.: Clear and cloudy sky investigations using RAMAN Lidar and airborne interferometric measures from the European AQUA Thermodynamic Experiment, Atmos. Res., in review, 2010. 7222, 7223

Masuda, K., Takashima, T., and Takayama, Y.: Emissivity of pure and sea waters for the model sea surface in the infrared window regions, Remote Sens. Environ., 24, 313–329, 1988. 7221

McGill, M. J., Hlavka, D. L., Hart, W. D., Scott, V. S., Spinhirne, J. D., and Schmid, B.: The Cloud Physics Lidar: instrument description and initial measurement results, Appl. Opt., 41, 3725–3734, 2002. 7219

Moeller, C. C., Revercomb, H. E., Ackerman, S. A., Menzel, W. P., and Knuteson, R. O.: Evaluation of MODIS thermal IR band L1B radiances during SAFARI 2000, J. Geophys. Res., 108, 1–12, 2003. 7220

NASA: MAS, available online at: http://mas.arc.nasa.gov/, last access: March 2010, 2008. 7222

NASA-GSFC: MODIS, available online at: http://modis.gsfc.nasa.gov/, last access: March 2010, 2008. 7233

Potter, J. F.: The delta function approximation in radiative transfer theory, J. Atmos. Sci., 27, 943–949, 1970. 7223

Revercomb, H. E., Walden, V. P., Tobin, D. C., Anderson, J., Best, F., Ciganovich, N. C., Dedecker, R. G., Dirkx, T., Ellington, S. C., Garcia, R. K., Herbsleb, R., Knuteson, R. O., LaPorte, D., McRae, D., and Werner, M.: Recent Results From Two New Aircraft-Based Fourier-Transform Interferometers: The Scanning High-resolution Interferometer Sounder and the NPOESS Atmospheric Sounder Testbed Interferometer, in: ASSFTS Conference, Toulouse, France, 1998. 7219

Rizzi, R. and Maestri, T.: Some considerations on far infrared emission in presence of clouds, J. Geophys. Res, 108, 4403–4408, 2003. 7218

Rizzi, R., di Pietro, P., Loffredo, G., and Smith, J. A.: Comparison of measured and modeled stratus cloud infrared spectral signatures, J. Geophys. Res., 106, 34109–34120, 2001. 7218

Rizzi, R., Maestri, T., and Bozzo, A.: Reference tool for simulation of VIS/NIR spectral radiances, Tech. rep., http://www.eumetsat.int/, EUMETSAT Contract EUM/CO/06/1529/PS, last access: March 2010, 2007. 7233

Rothman, L. S., Jacquemart, D., Barbe, A., Chris Benner, D., Birk, M., Brown, L. R., Carleer, M. R., Chackerian, C., Chance, K., Coudert, L. H., et al.: The HITRAN 2004 molecular spectroscopic database, J. Quant. Spectrosc. Ra., 96, 139–204, 2005. 7221

Takano, Y. and Liou, K. N.: Solar radiative transfer in cirrus clouds. Part I: Theory and computation of multiple scattering in anisotropic medium, J. Atmos. Sci., 46, 20–36, 1988. 7223

Tjemkes, S. A., Patterson, T., Rizzi, R., Shephard, M. W., Clough, S. A., Matricardi, M., Haigh, J. D., Höpfner, M., Payan, S., Trotsenko, A., Scott, N., Rayer, P., Taylor, J., Clerbaux, C., Strow, L. L., DeSouza-Machado, S., Tobin, D., and Knuteson, R.: The ISSWG line-by-line inter-comparison experiment, J. Quant. Spectrosc. Ra., 77, 433–453, 2003. 7218

Turner, D. D. and Eloranta, E. W.: Validating mixed-phase cloud optical depth retrieved from infrared observations with high spectral resolution lidar, IEEE Geosci. Remote Sens., 5, 285–288, doi:10.1109/LGRS.2008.915940, 2008. 7237

Vermote, E. F., Tanré, D., Deuzé, J. L., Herman, M., Morcrette, J. J., and Kotchenova, S. Y.: Second Simulation of a Satellite Signal in the Solar Spectrum-Vector (6SV), available at: http://6s.ltdri.org, last access: March 2010, 2006. 7222

Wendisch, M., Pilewskie, P., Pommier, J., Howard, S., Yang, P., Heymsfield, A. J., Schmitt, C. G., Baumgardner, D., and Mayer, B.: Impact of cirrus crystal shape on solar spectral irradiance: A case study for subtropical cirrus, J. Geophys. Res., 110, d03202, doi:10.1029/2004JD005294, 2005. 7222

Wyser, K.: Ice crystal habits and solar radiation, Tellus A, 51, 937–950, 1999. 7222

Xie, Y., Yang, P., Kattawar, G. W., Minnis, P., and Hu, Y. X.: Effect of the inhomogeneity of ice crystals on retrieving ice cloud optical thickness and effective particle size, J. Geophys. Res, 114, D11203, doi:10.1029/2008JD011216, 2009. 7238

Yang, P. and Liou, K. N.: Single scattering properties of complex ice crystals in terrestrial atmosphere, Contrib. Atmos. Phys., 71, 223–248, 1998. 7222

Yang, P., Wei, H., Huang, H.-L., Baum, B. A., Hu, Y. X., Kattawar, G. W., Mishchenko, M. I., and Fu, Q.: Scattering and absorption property database for non-spherical ice particles in the near through far infrared database, Appl. Optics, 44, 5512–5523, 2005. 7222

Yang, P., Zhang, L., Hong, G., Nasiri, S. L., Baum, B. A., Huang, H., King, M. D., and Platnick, S. E.: Differences Between Collection 4 and 5 MODIS Ice Cloud Optical/Microphysical Products and Their Impact on Radiative Forcing Simulations, IEEE T. Geosci. Remote, 45, 2886, doi:10.1109/TGRS.2007.898276, 2007. 7217

Yang, P., Hong, G., Kattawar, G. W., Minnis, P., and Hu, Y.: Uncertainties Associated With the Surface Texture of Ice Particles in Satellite-Based Retrieval of Cirrus Clouds: Part II–Effect of Particle Surface Roughness on Retrieved Cloud Optical Thickness, IEEE T. Geosci. Remote, 46, 1948–1957, 2008a. 7238

Yang, P., Kattawar, G. W., Hong, G., Minnis, P., and Hu, Y.: Uncertainties Associated With the Surface Texture of Ice Particles in Satellite-Based Retrieval of Cirrus Clouds–Part I: Single-Scattering Properties of Ice Crystals With Surface Roughness, IEEE T. Geosci. Remote, 46, 1940–1947, 2008b. 7238

Zhang, Z., Yang, P., Kattawar, G., Riedi, J., -Labonnote, L. C., Baum, B. A., Platnick, S., and Huang, H.-L.: Influence of ice particle model on satellite ice cloud retrieval: lessons learned from MODIS and POLDER cloud product comparison, Atmos. Chem. Phys., 9, 7115–7129, 2009, http://www.atmos-chem-phys.net/9/7115/2009/. 7217, 7238

Table 1. Characteristics of the 3 cloudy sectors used for the comparisons. CPL OT is optical thickness measured by CPL at 532 nm and CPL OT 1σ is the standard deviation of measured CPL OT in each sector; RT-RET OT and effective diameter (D_e) are retrieved from S-HIS data averaged in each sector; CLT and CLB are cloud top and bottom height obtained from CPL.

Case	CPL OT 532 nm	CPL OT 1σ	RT-RET OT 532 nm	RT-RET OT 1000 cm^{-1}	D_e µm	CLT km	CLB km
Sector 1	0.56	0.3	0.57	0.53	68	11.6	9.7
Sector 2	0.91	0.4	1.02	0.95	64	11.9	9.8
Sector 3	2.94	0.02	2.99	2.80	80	12.1	10.0

ACPD
10, 7215–7264, 2010

Table 2. Relevant parameters and retrieved cloud properties for the three areas selected for the MODIS case studies (the name is defined in column one) over the cirrus cloud of Fig. 15. SUN z.a. is the solar zenith angle; Azi. and Zen. are the azimuth and zenith observation angles; CTP, OT and R_e are the MODIS retrieved cloud top pressure, optical thickness and effective radius; OT 1σ is estimated error on OT. IWC is cloud ice water content and CD is assumed cloud layer depth.

Area	Sun z.a.	Azi.	Zen.	CTP hPa	OT	OT 1σ %	R_e µ	IWC kg/m^3	CD m
Ci1	42.5	45	31	340	4	8	44	0.027	3790
Ci2	42.5	43	30	330	11	10	38	0.064	3790
Ci3	42.5	41	42	260	20	18	30	0.103	3790

Table 3. MODIS bands used for the comparison, listed for increasing wavelength. BW is the bandwidth defined by the 1% points in the L1B in-band RSR.

Band	CW nm	BW nm
B3	465.6	17.6
B4	553.7	19.7
B1	646.5	41.8
B2	856.7	39.4
B17	904.1	35.7
B18	935.3	13.7
B19	936.1	46.3
B6	1629.1	29.7
B7	2114.3	52.9

ACPD
10, 7215–7264, 2010

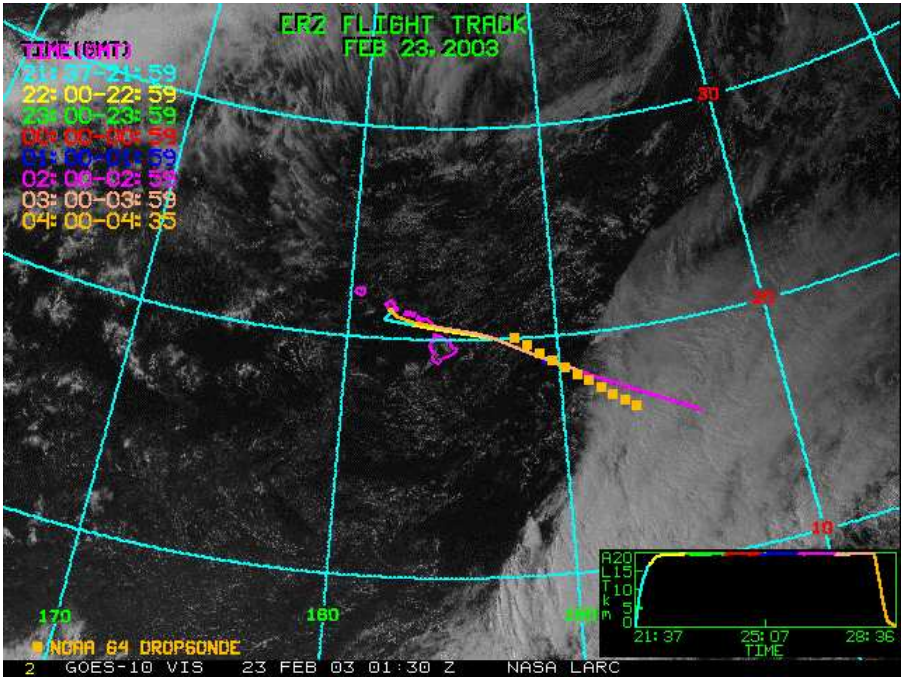

Fig. 1. GOES-10 visible channel image, 23 February 2003. ER-2 route and the drop-sondes positions are shown (from http://www-angler.larc.nasa.gov/thorpex/).

ACPD
10, 7215–7264, 2010

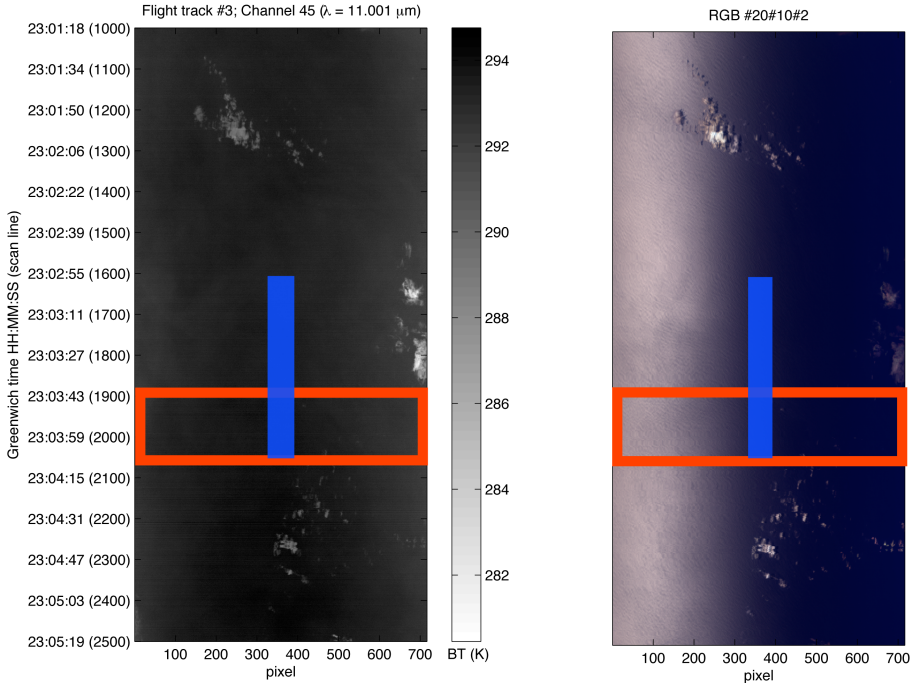

Fig. 2. MAS imagery on Pacific Ocean SE from Hawaiian Islands on 22 February 2003, from 23:01 to 23:05 UTC (roughly 50 km on the ground). Infrared brightness temperature from channel 45 (11 μm) is presented on left panel. RGB image (right panel) is obtained from channels 20 (2.15 μm), 10 (1.64 μm), 2 (0.55 μm). The blue line and the red box show the regions chosen for the cross-scan and nadir comparisons.

ACPD
10, 7215–7264, 2010

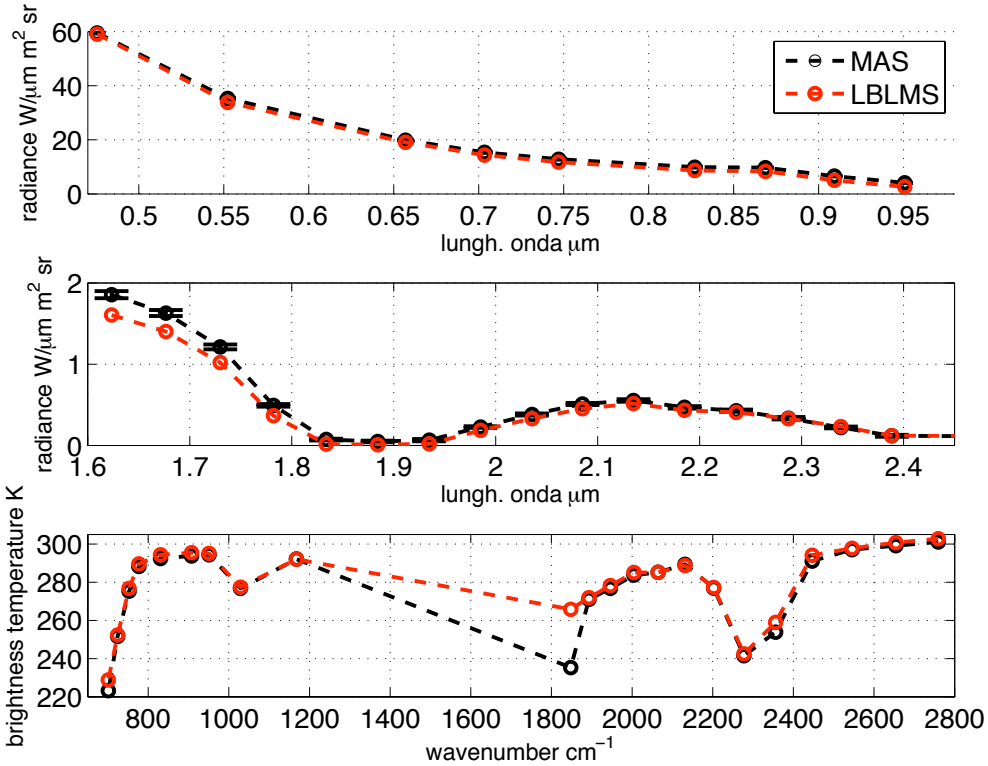

Fig. 3. Comparison of LBLMS simulations and MAS observation at nadir in clear sky conditions. Top and mid panel: comparison between measured and simulated upwelling radiance at 20 km; lower panel: IR brightness temperature.

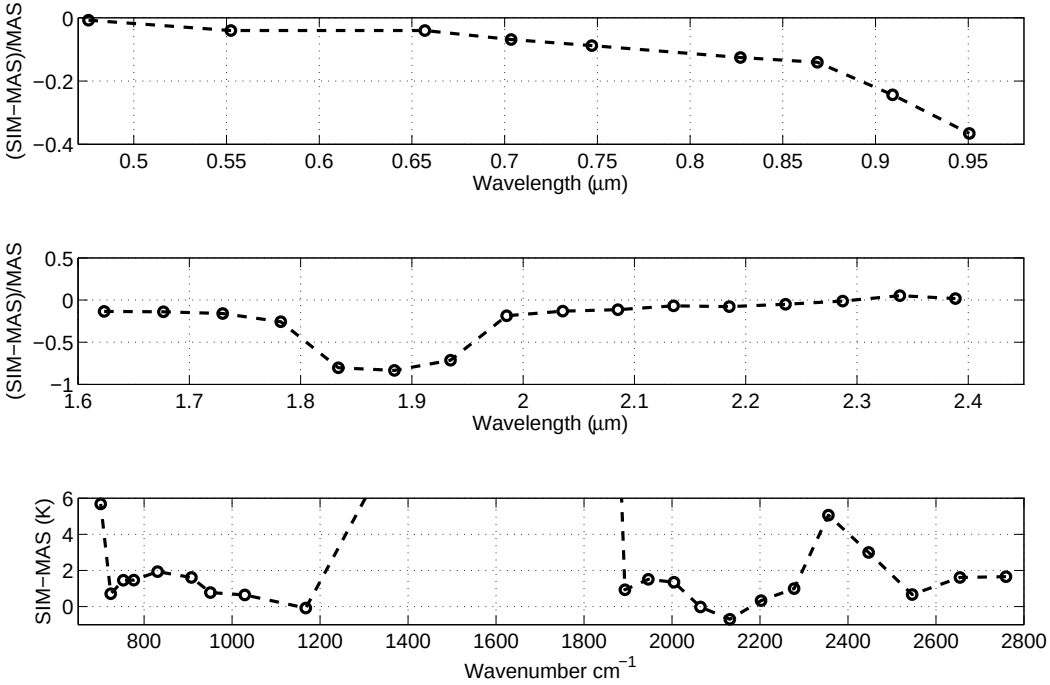

Fig. 4. Differences between LBLMS simulations and MAS observation at nadir in clear sky conditions. Top and mid panel: relative radiance errors (LBLMS-MAS)/MAS; lower panel:-absolute IR brightness temperature difference (LBLMS-MAS, K).

ACPD
10, 7215–7264, 2010

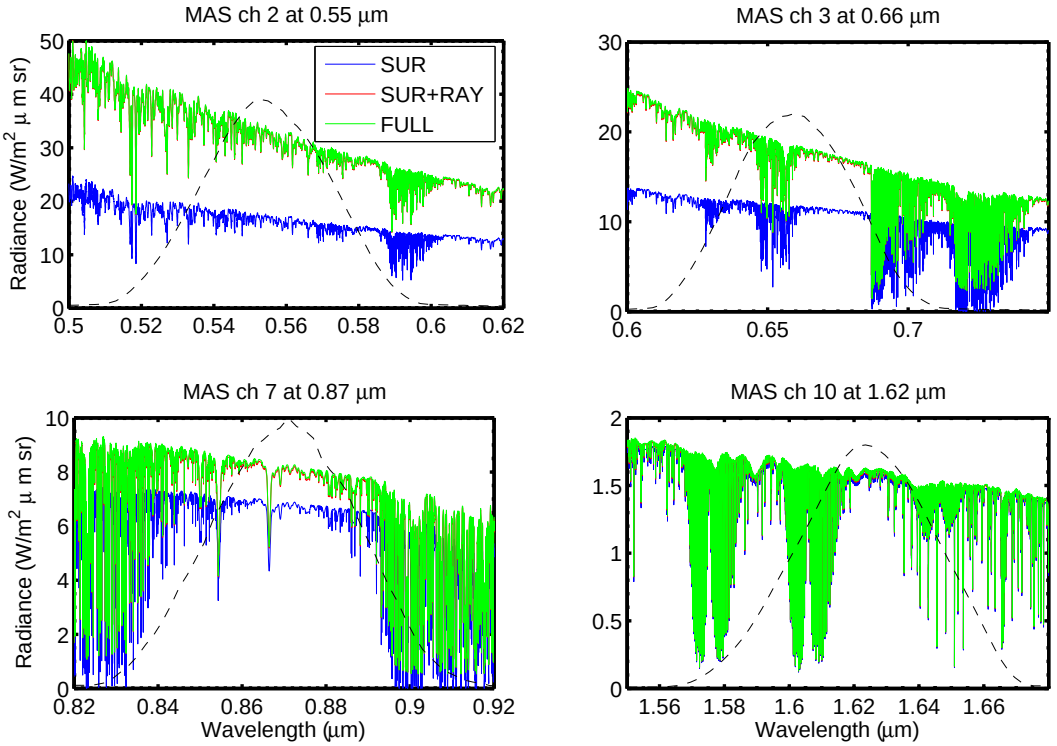

Fig. 5. High resolution spectral radiance in four MAS channels: channel 2 (top left), channel 3 (top right), channel 7 (bottom left) and channel 10 (bottom right). The colour coding is same for all the panels: the blue line labeled SUR is the case when the surface is the sole source function with a molecular atmosphere that only absords radiance; the red curve labeled (SUR+RAY) is radiance after molecular scattering is added; the green line (FULL) considers also the presence of aerosol as source function and absorber. The dashed black line is MAS Relative Response Function on a relative scale.

ACPD
10, 7215–7264, 2010

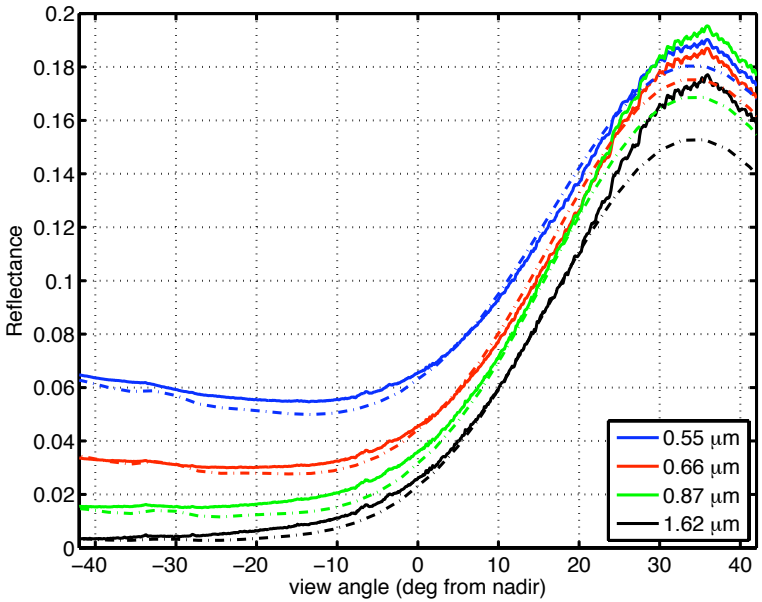

Fig. 6. Reflectance comparison between LBLMS (dashed lines) and MAS (continuous lines) along a MAS scan. Wind speed is 6.5 m/s, aerosol OD at 532 nm 0.07 and pigment concentration 0.07 mg/m^3.

ACPD
10, 7215–7264, 2010

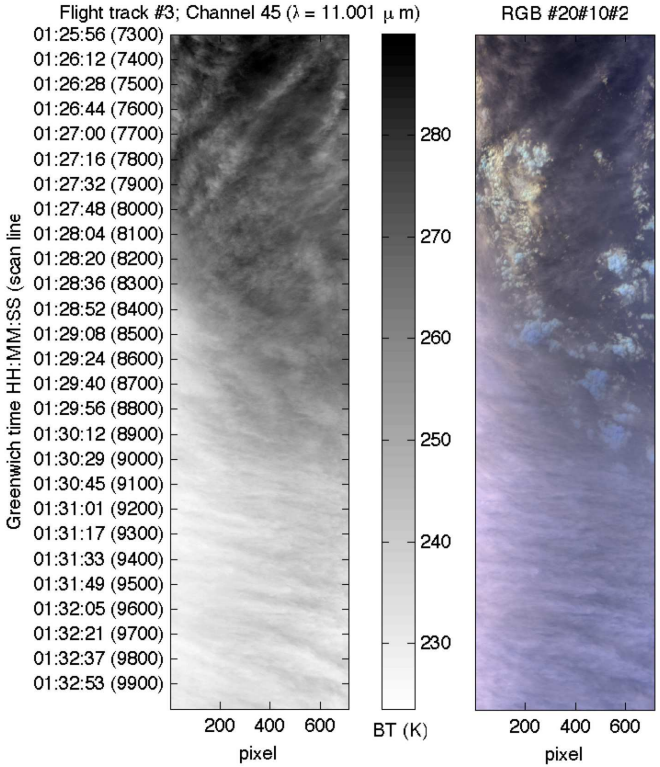

Fig. 7. Cloudy sky scenario. MAS imagery from track 9, 23 February 2003 on Pacific Ocean SE from Hawaiian Islands from 01:26 to 01:33 UTC. Infrared brightness temperature from channel 45 is presented on left panel. RGB image (right panel) is obtained from channels 20 (2.15 μm), 10 (1.64 μm), 2 (0.55 μm).

ACPD
10, 7215–7264, 2010

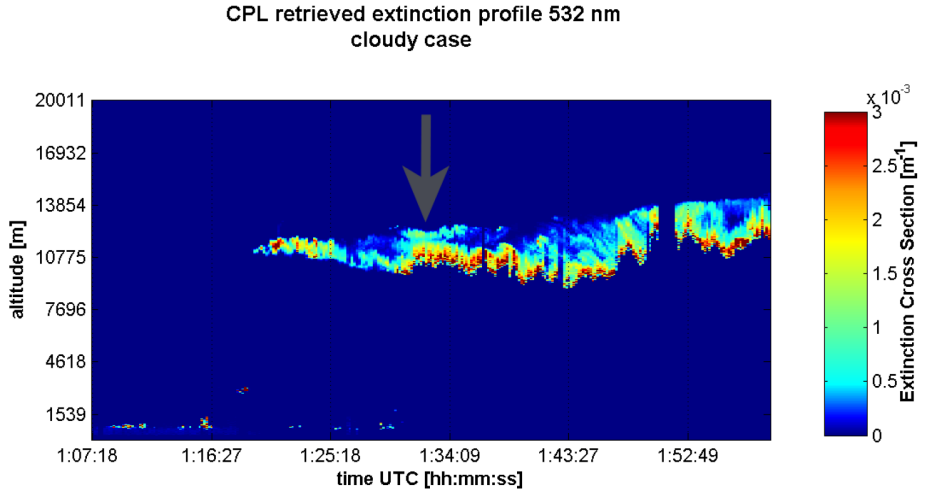

Fig. 8. CPL extinction cross section from 01:07 to 01:54 UTC on the 23 February 2003.

ACPD
10, 7215–7264, 2010

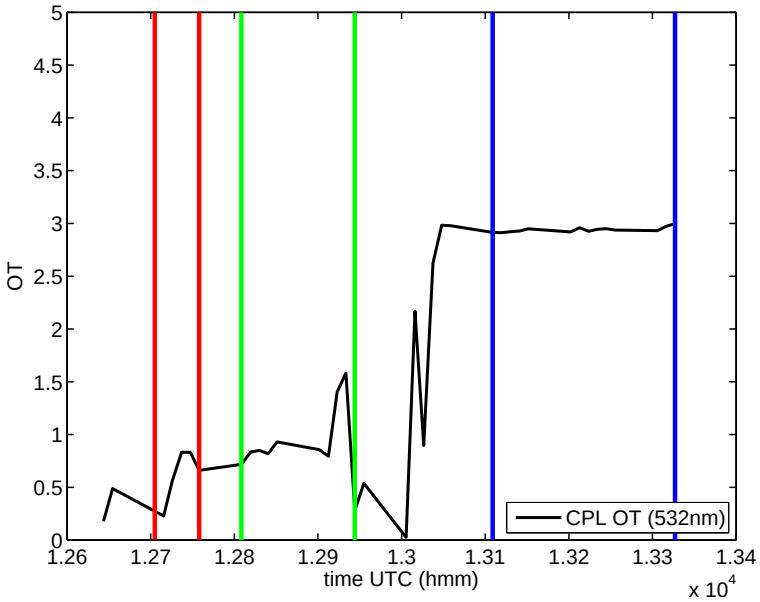

Fig. 9. CPL retrieved cloud total optical depth for the ER-2 flight leg from 01:26 to 01:34 UTC, 23 February 2003. The vertical coloured lines delimitate the three sectors selected for the comparisons.

ACPD
10, 7215–7264, 2010

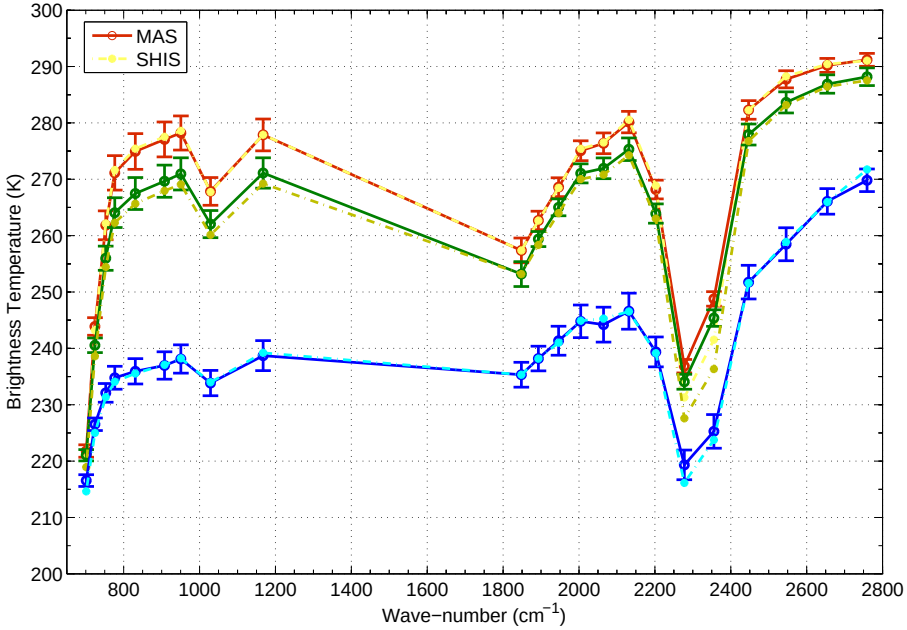

Fig. 10. MAS data averaged over S-HIS nadir FOV and S-HIS data convolved with MAS relative spectral response. The red solid line and yellow dashed refer to Sector 1 (the thin cloud layer); the two green shades are for Sector 2 (medium cloud layer) and the blue lines are for the moderately thick layer of Sector 3. The vertical bars are the one standard deviation of the MAS data around the average values and denote the natural variability as well as radiometric error.

ACPD
10, 7215–7264, 2010

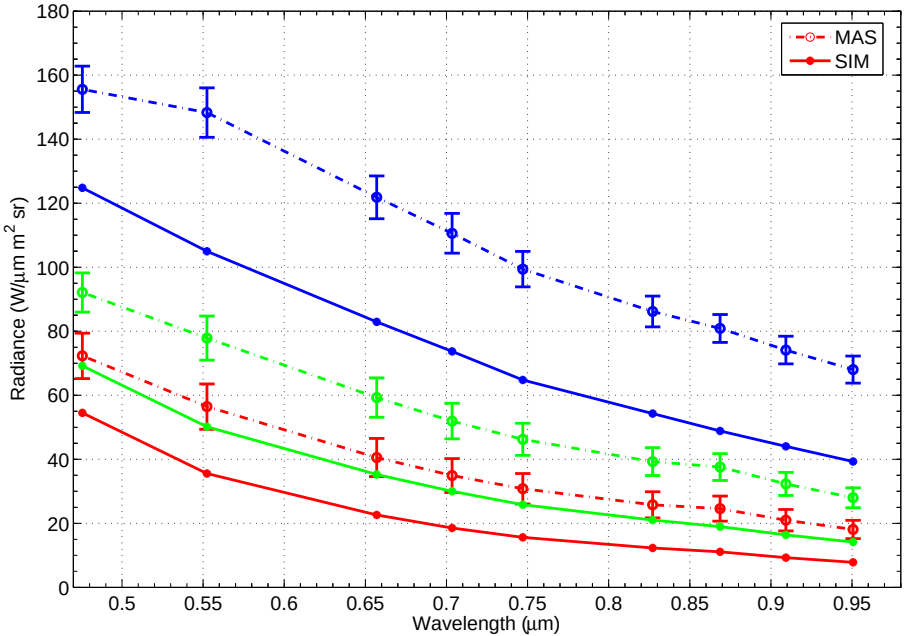

Fig. 11. LBLMS simulations and MAS observations in cloudy conditions – SW range. The three colours represent the three sections highlighted in Fig. 9: red for the thin cloud layer, green for the medium cloud layer and blue for the moderately thick layer. The vertical bars have same meaning as in Fig. 10.

ACPD
10, 7215–7264, 2010

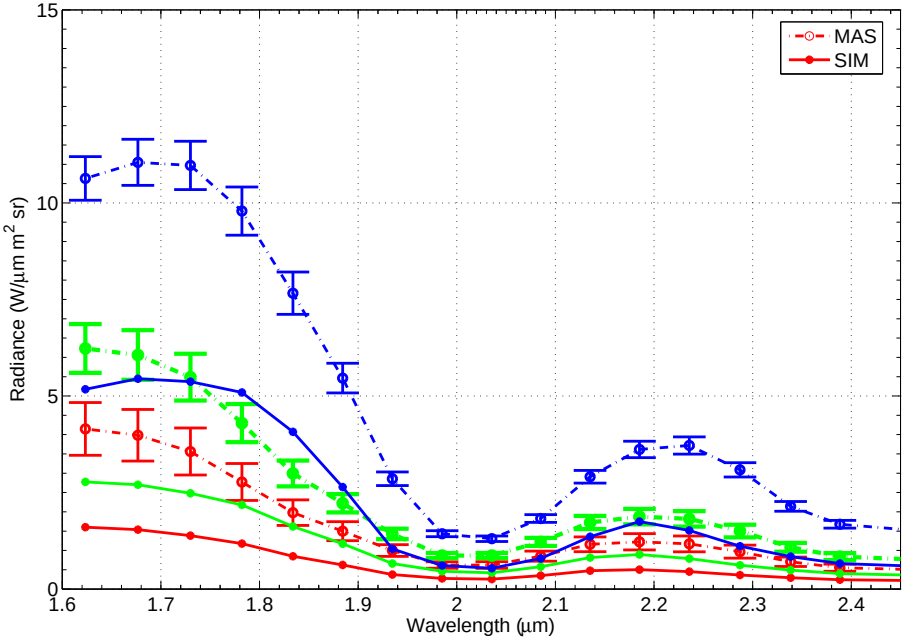

Fig. 12. Same as Fig. 11 but for the NIR spectral range.

ACPD
10, 7215–7264, 2010

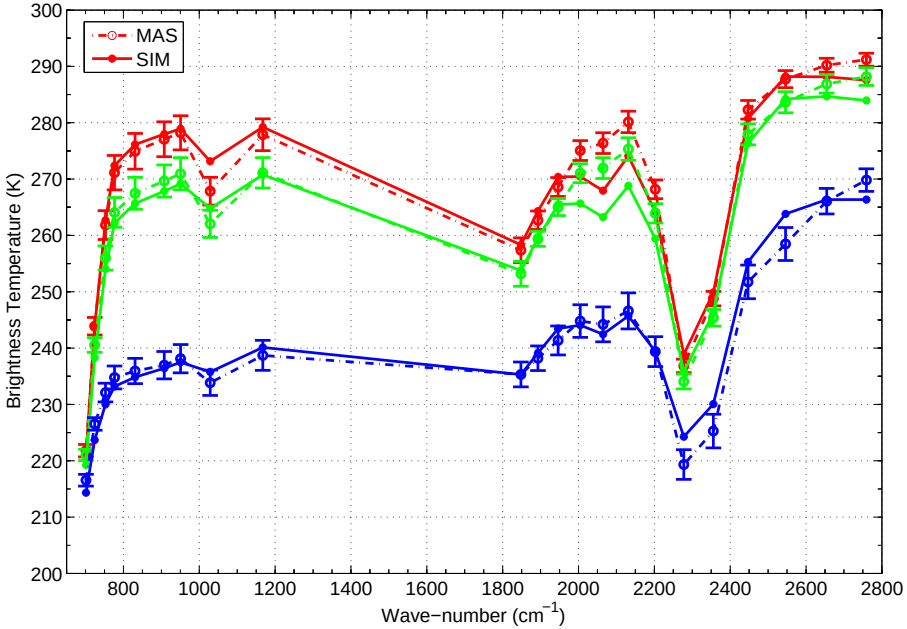

Fig. 13. IR brightness temperature from LBLMS simulated and MAS observed radiance at 20 km. The three colours represent the three sections highlighted in Fig. 9. The vertical bars have same meaning as in Fig 10.

ACPD
10, 7215–7264, 2010

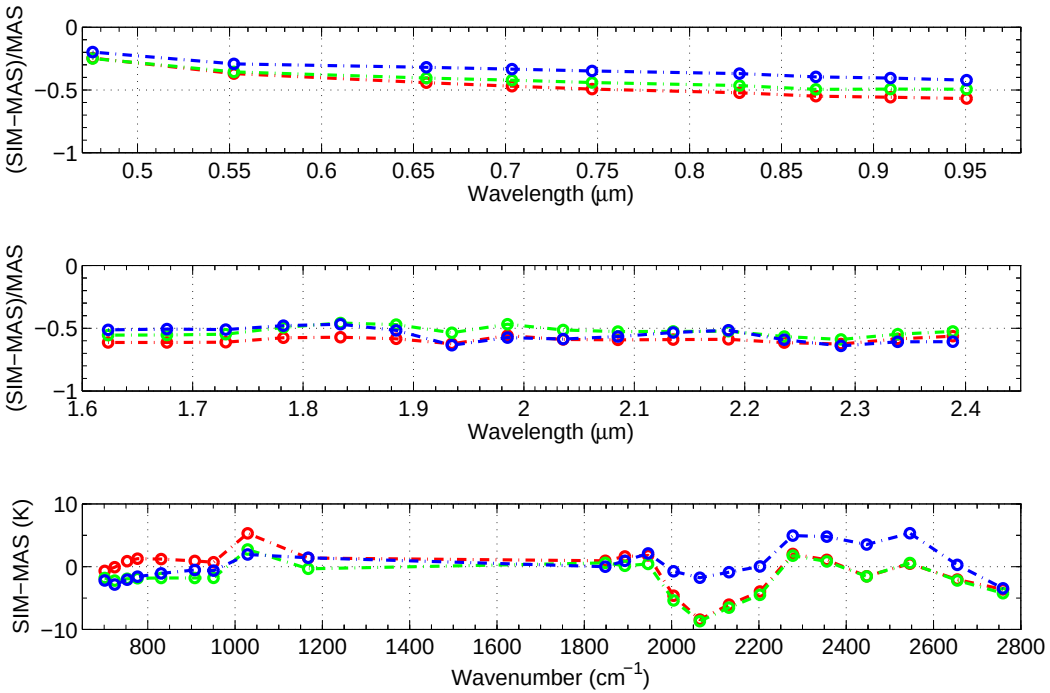

Fig. 14. Differences between LBLMS simulations and MAS observation in cloudy conditions. Top and mid panel: relative radiance errors (LBLMS-MAS)/MAS; lower panel: absolute IR brightness temperature difference (LBLMS-MAS, K). The three colours represent the three sections highlighted in Fig. 9.

ACPD
10, 7215–7264, 2010

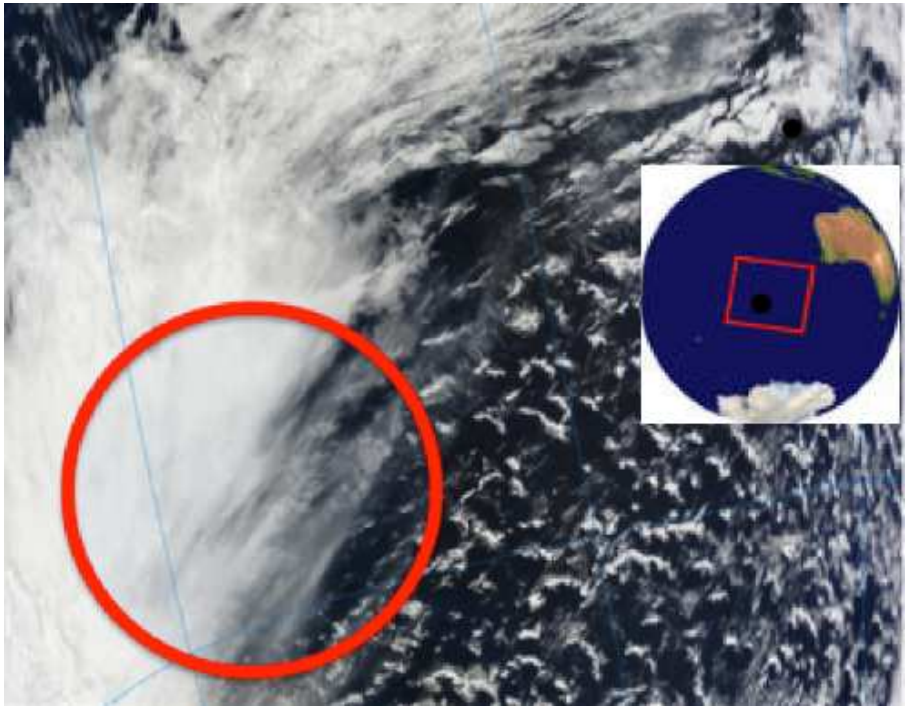

Fig. 15. MODIS RGB image of the scenario used for the comparison with LBLMS. The red circle highlights the cloudy regions used for the test.

ACPD

10, 7215–7264, 2010

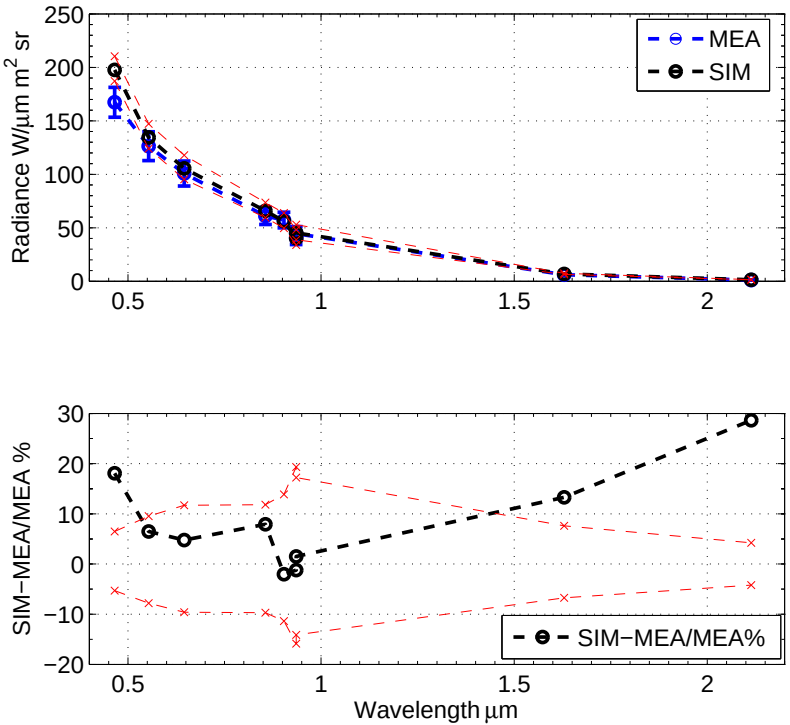

Fig. 16. LBLMS and MODIS radiances for Area Ci1. Upper panel: the blue dashed line connects measured MODIS values (open blue circles); the blue bars denote the (2σ) variability around the mean measured radiance corresponding to same retrieved OT for the Area; the black dashed line connects the simulated values (open black circles); the dashed red lines are the radiance computed with OT varied by twice the 1σ value given in Table 5 and thus denote the 2σ uncertainty level. Lower panel: relative percent difference (black dashed line and open circles); the red dashed lines are the 2σ uncertainty level.

ACPD
10, 7215–7264, 2010

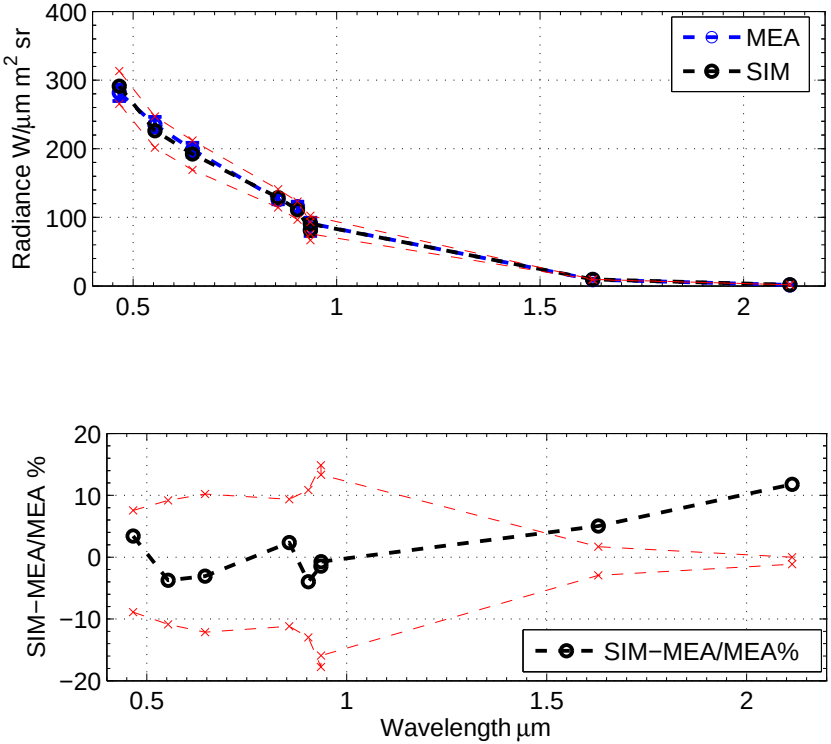

Fig. 17. Same as Fig. 16 but for Area Ci2.

ACPD
10, 7215–7264, 2010

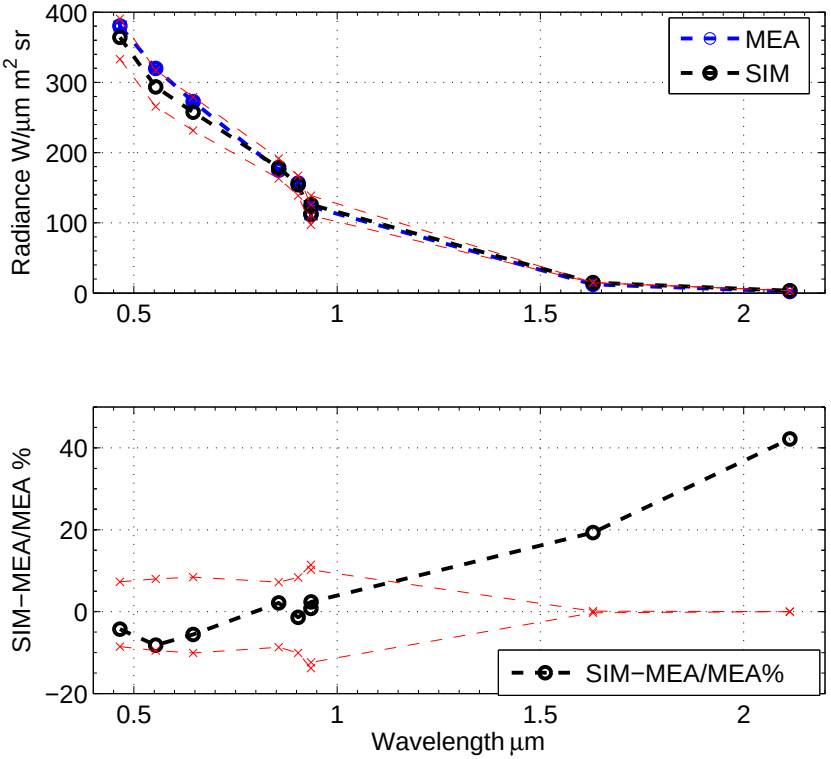

Fig. 18. Same as Fig. 16 but for Area Ci3.

ACPD
10, 7215–7264, 2010